Geophysical Journal International

Geophys. J. Int. (2014) **199,** 1214–1229 doi: 10.1093/gji/ggu300

GJI Geomagnetism, rock magnetism and palaeomagnetism

Magnetic fabrics induced by dynamic faulting reveal damage zone sizes in soft rocks, Dead Sea basin

T. Levi,[1] R. Weinberger[1,2] and S. Marco[3]

[1]*Geological Survey of Israel,* 30 *Malkhe Yisrael Street, Jerusalem* 95501*, Israel. E-mail: tsafrir@gsi.gov.il*

[2]*Department of Geological and Environmental Sciences, Ben-Gurion University of the Negev, Beer-Sheva* 84105*, Israel*

[3]*Department of Geophysics and Planetary Sciences, Tel Aviv University, Tel Aviv* 69978*, Israel*

Accepted 2014 July 29. Received 2014 July 28; in original form 2013 October 2

SUMMARY

The anisotropy of magnetic susceptibility (AMS) of soft rocks was measured in order to distinguish between the effect of remote and local strain fields, determine the size of the related inelastic damage zone and resolve the fault-plane solutions of past earthquakes. The AMS fabrics were explored next to late Pleistocene syndepositional normal faults (total displacement up to ∼3.5 m) that cross soft lacustrine rocks within the seismically active Dead Sea basin. 'Deposition fabrics' prevail meters away from the fault planes and are characterized by scattered maximum and intermediate principal AMS axes. 'Deformation fabrics' are detected up to tens of centimetres from the fault planes and are characterized by well-grouped AMS axes, in which one of the principal axes is parallel to the strike of the nearby fault. Variations in the AMS fabrics and magnetic lineations define the size of the inelastic damage zone around the faults. The results demonstrate that the deformation-driven magnetic fabrics and the associated inelastic damage zones are compatible with coseismic dynamic faulting and the effects of the local strain field during earthquakes. Most of the AMS fabrics show a conspicuous similarity to that of the fault-plane solutions, i.e., the principal AMS axes and instantaneous strain ellipsoids are coaxial. These results suggest a novel application of the AMS method for defining the shape and size of the damage zones surrounding dynamic faults and determining the full tensor of the local strain field.

Key words: Magnetic fabrics and AMS; Palaeoseismology; Fractures and faults.

1 INTRODUCTION

An earthquake is an expression of a sudden release of remote tectonic strain that accumulates during relative plate motions. During a seismic event, the stored elastic and inelastic strains are released dynamically by fast faulting and spreading of acoustic waves through the medium (e.g. Shearer 1999). The principal axes of the remote tectonic strain (i.e. far-field strain) can be considered approximately constant over a hundred of kilometres in certain region and several earthquake cycles. In such a case, the strain field is commonly determined by analysis of the fault-plane and moment tensor solutions of a large group of earthquake events or by analysis of mesoscale kinematic indicators (e.g. fault-plane solutions utilizing striations on small faults). However, the principal axes of the local strain field (i.e. near-field strain) released during individual earthquake events may vary up to several kilometres from the fault planes (e.g. Ma & Andrews 2010). They can be determined by calculations of the moment tensor solutions based on recordings of the direction and time of arrival of *P* waves in seismic stations adjacent to the active fault strands (e.g. Yukutake *et al.* 2010), or by simulations with various mechanical models (e.g. Rice *et al.* 2005; Fukuyama 2009, and references therein).

During the faulting, a recoverable elastic deformation and partially unrecoverable inelastic deformation evolve. Usually the inelastic deformation is expressed by an envelope of deformed volume around the faults, known as a damage zone. This zone includes a wide variety of structures that span from micron to meter scales (Chester & Logan 1986; Weinberger *et al.* 2000; Shipton & Cowie 2003; Schultz & Fossen 2008; Braathen *et al.* 2009; Faulkner *et al.* 2011, and references therein). The damage zone has received a lot of attention over the years, as it is a key component in the energy balance of earthquake and faulting mechanisms (Rice *et al.* 2005; Ma & Andrews 2010).

Determining the size of the damage zone near faults is important for understanding the mechanism of fault propagation during brittle fracturing and the earthquake process at the upper crust (Lyakhovsky & Ben-Zion 2008). The decay of damage zones with distance from fault planes is related to the decline of the strain field away from the faults, as is predicted by fracture mechanics models (e.g. Scholz 2002). Despite the importance in determining the size

of the damage zones, it is difficult to distinguish between the effect of the remote and the local strain fields close to fault planes. This difficulty arises because the local strain field is likely to be complex compared to the remote strain field; in some places close to the fault planes the mesoscale kinematic indicators are absent, and it is not always clear which structural characteristics determine the size of the damage zones.

Aiming to overcome the above difficulty, we analyse the anisotropy of magnetic susceptibility (AMS) of soft rocks next to normal faults. In many deformed environments, the principal AMS axes are coaxial with the directions of the principal strain axes (Borradaile 1987, 1991; Borradaile & Henry 1997; Mattei *et al.* 1997; Parés *et al.* 1999; Hirt *et al.* 2000; Cifelli *et al.* 2005; Latta & Anastasio 2007; Soto *et al.* 2007; Hrouda *et al.* 2009; Borradaile & Jackson 2010; Porreca & Mattei 2012). The AMS generally reflects the inelastic strain preserved in the rocks in the form mainly of lattice distortion and crystallographic axis rotations (e.g. Borradaile & Henry 1997). Lineations and foliations of magnetic fabrics may form as a result of sedimentary processes such as deposition and compaction (Hrouda 1982; Taira 1989; Tarling & Hrouda 1993) and transport of clastics (e.g. Rees 1971; Rees & Woodall 1975; Liu *et al.* 2001; Levi *et al.* 2006b).

Magnetic fabrics in soft sediments may be developed under different sedimentary environments such as marine coastal settings, tidal bore in estuarine settings, or in bottom lake environments (e.g. Beck 2009). Under instability triggered by an earthquake or pore-water pressure increases, the column sediments can be transported and associated with various types of deformed structures (e.g. 'ball-and-pillow' like structures, slumps and brecciated layers; see Marco & Agnon 2005; Beck 2009).

Tectonic AMS subfabrics may develop during progressive deformation under regional shortening (Kissel *et al.* 1986) or elongation (e.g. Cifelli *et al.* 2005) or crenulation formation (e.g. Porreca & Mattei 2012). Such subfabrics obliterate the primary sedimentary magnetic fabric, according to the nature and extent of the deformation (e.g. Borradaile 1991; Parés *et al.* 1999; Housen & Kanamatsu 2003; Parés & Van der Pluijm 2003; Schwehr & Tauxe 2003; Aubourg *et al.* 2010; Larrasoaña *et al.* 2011; Levi & Weinberger 2011; Cifelli *et al.* 2013, among many others). Hence, magnetic lineations and foliations begin to develop during progressive deposition and deformation, preserving inelastic strain stored in the rocks.

The determination of whether the magnetic fabrics near fault planes are a direct product of dynamic faulting events (i.e. local strain field) or the consequence of a long period of tectonic activity (i.e. remote strain field) is yet unclear. If the AMS fabrics are associated with the faulting, they could represent the spatial distribution of the local strain field, be applied to determine the extent of the inelastic damage zone that develops during the fault activity, and also could be useful in determining the fault-plane solutions of past earthquake events.

The development of AMS fabrics may take hundreds of thousands of years during protracted geological processes such as deposition, compaction and lithification (García-Lasanta *et al.* 2013) or folding. Larrasoaña *et al.* (2011) show that in Lake Issyk-Kul in the Kyrgyz Tien Shan fold-and-thrust belt the tectonic AMS fabrics were rapidly locked, shortly (~dozens of years) after sediment deposition during the Late Holocene. Borradaile & Hamilton (2004) suggest that the AMS fabrics are comparable to fault-plane solutions for recent earthquakes in the Polis rift, NW Cyprus. In this context, Aubourg *et al.* (2004) compare the AMS fabrics from Zagros-Makran block (Iran) to the directions of *P*-axes of fault-plane solutions in this region. In western part and southeastern parts of the block they found good agreement between the AMS axes and *P*-axes directions. However, in some parts of the study area Aubourg *et al.* (2004) find a contrasting pattern between the AMS shortening directions and the *P*-axes directions, suggesting that the AMS recorded a longer deformation history compared to that of the recent seismic activity. Nevertheless, the distinction between magnetic fabrics associated with the remote strain fields and those associated with earthquake-driven local strain fields is still questionable.

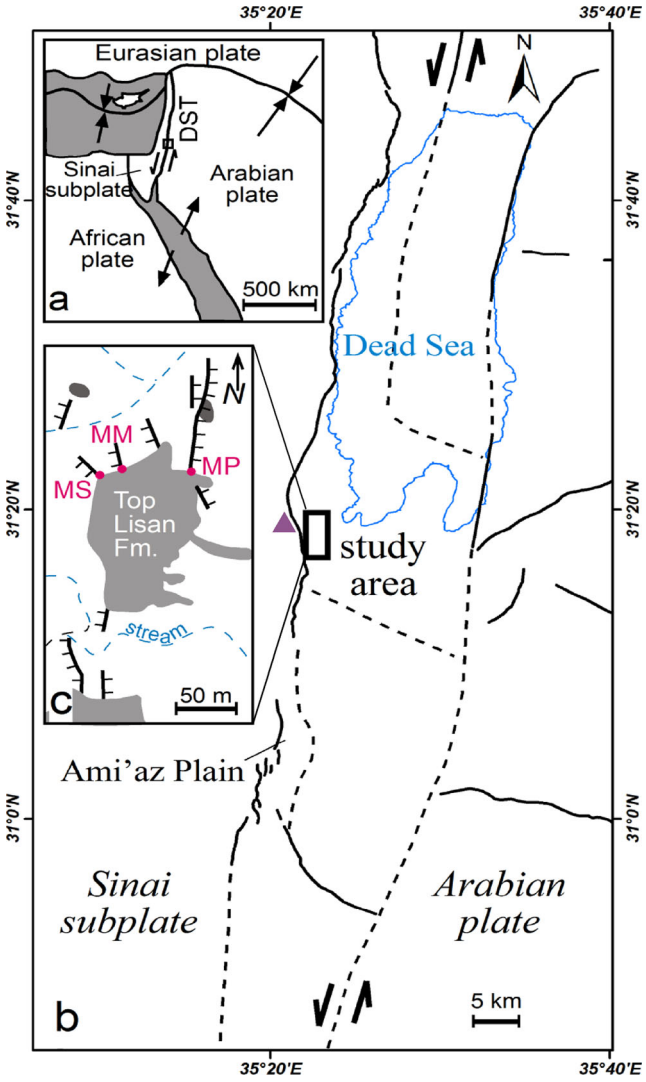

Figure 1. Location maps: (a) plate tectonic configuration resulting in a left-lateral motion across the Dead Sea transform (DST), (b) regional setting of the Dead Sea basin. Fault map is based on Sneh & Weinberger (2014). Masada Plain is marked by rectangle. Solid lines – main faults at the surface; dashed lines – main faults at the subsurface; purple triangle – Masada, world heritage site and (c) detailed fault map at the study area (after Marco & Agnon 2005). AMS sampling sites MS, MM and MP are marked with red circles.

In this study, we explore the development of magnetic fabrics close to three well-documented faults that cross late Pleistocene soft rocks in the Masada Plain, Israel (Marco & Agnon 2005), within the seismically active Dead Sea basin (Fig. 1). We identify the relations between the faulting processes and magnetic fabrics, provide a method for characterizing the size of the inelastic damage

zone next to faults, and propose that the magnetic fabrics resemble the fault-plane solutions of past earthquakes.

2 MAGNETIC FABRICS NEXT TO FAULT PLANES

We use AMS fabrics to distinguish between four different settings (Table 1), two of which are associated with sedimentary processes (Rees 1971; Rees & Woodall 1975; Tauxe 1998; Levi *et al.* 2006b; García-Lasanta *et al.* 2013) and the other two with deformation processes (Borradaile & Henry 1997; Borradaile & Jackson 2010; Levi & Weinberger 2011). By elucidating changes in the AMS fabrics within fault zones and away from them (i.e. far and near zones), we can further differentiate between the effect of remote and local strain fields and document fabrics preserved in soft sedimentary rocks (Fig. 2).

AMS is described by three principal axes, k_{max} (k_1), k_{int} (k_2) and k_{min} (k_3), which correspond to the maximum, intermediate and minimum magnetic susceptibility magnitudes, respectively. Statistically, the principal AMS axes of a number of samples are displayed with their associated 95 per cent confidence ellipses (Jelinek 1978) and the bootstrapped confidence limits (Tauxe *et al.* 1991). In *setting* 1, the particles are settled and scattered on the bedding planes, and the AMS fabric is characterized by well-grouped vertical k_3 axes and scattered k_1 and k_2 axes along the girdle. Under these conditions, the 95 per cent confidence regions of k_1 and k_2 axes are relatively large and overlap. In *setting* 2 the particles are transported by currents towards the depocentre, and due to particle alignment the AMS fabric is characterized by well-grouped subvertical k_3 axes and weakly clustered subhorizontal k_1 and k_2 axes. Under conditions of laminar and slow currents with transported prolate particles (or spherical, but aligned along a certain line) above the bottom of the lake, which slopes down moderately, k_1 axes are expected to be parallel to the transport direction (Rees & Woodall 1975; Hrouda 1982; Taira 1989; Tauxe 1998) and the 95 per cent confidence ellipses of k_1, and k_2 may be relatively large. We hypothesize that *settings* 1 and 2, which are associated with sedimentary processes, will be diagnostic for the sedimentary rocks throughout the entire region (Fig. 2).

In *setting* 3 the remote tectonic strain (stress) field aligns the particles such that k_3, k_2 and k_1 axes are well grouped and coaxial with the remote maximum (ε_1), intermediate (ε_2) and minimum (ε_3) shortening axes, respectively. If the remote strain field is dominant and obliterates an original fabric, the resulting fabric is expected to be similar everywhere, without relation to the distance from the fault planes. In *setting* 4 the local strain field is dominant and aligns the particles such that k_1, k_2 and k_3 axes are well-grouped close to the fault planes. The resulting 'deformation fabrics' is characterized by either k_1 or k_2 axes parallel to the strike of the nearby fault; away from the fault planes, the original fabrics are not obliterated (Fig. 2). Because the local strain field often varies close to the fault planes, the AMS fabrics within a damage zone may change from one place to another (e.g. Ma & Andrews 2010). Under deformation conditions (*settings* 3 and 4), the 95 per cent confidence ellipses of k_1, k_2 and k_3 axes are relatively small and well-isolated from each other. Nevertheless, if only ε_1 or ε_3 axes are dominant (uniaxial strain), the 95 per cent confidence regions of

Table 1. Characterizations of AMS fabrics and their associated geological setting.

Geologic settings		Cause of anisotropy	Fabric characteristics	Statistics	Distribution area	Relation to faults	Distinct directions of AMS axes	Characterizations of the region	Remarks
Sedimentation conditions	Setting 1	Deposition of particles	Well-grouped vertical k_3 axes, scattered k_1 and k_2 axes along the girdle.	95% confidence ellipses of k_1 and k_2 axes are relatively large and overlapped	Everywhere	None	Vertical k_3	Lacustrine environment	Termed "deposition fabric"
	Setting 2	Transport of clastics toward the depocenter	Well-grouped sub-vertical k_3 axes, weakly-grouped k_1 and k_2 axes along the girdle.	95% confidence ellipses of k_1 and k_2 axes are relatively large	Vast areas	None	k_1 axes parallel to the transport direction	Lake depocenter is directed eastward	Termed "flow fabric"
Deformation conditions	Setting 3	Deformation – effect of remote strain	Well-grouped k_1, k_2 and k_3 axes.	95% confidence ellipses of k_1, k_2 and k_3 are relatively small and well-isolated from each other	Everywhere	Yes - to a large set of faults	Principal AMS and remote strain axes are coaxial	Maximum horizontal remote compression is ~340° - 160°	Termed "deformation fabric" and obliterate previous fabrics
	Setting 4	Deformation – effect of local strain	Well-grouped k_1, k_2 and k_3 axes.	95% confidence ellipses of k_1, k_2 and k_3 are relatively small and well-isolated from each other	Damage zones near individual faults	Yes - to individual faults	Principal AMS and local strain axes are coaxial, k_1 or k_2 axes parallel to fault strike	Faults strikes are 310°, 330° and 030°	Termed "deformation fabric" and obliterate previous fabrics

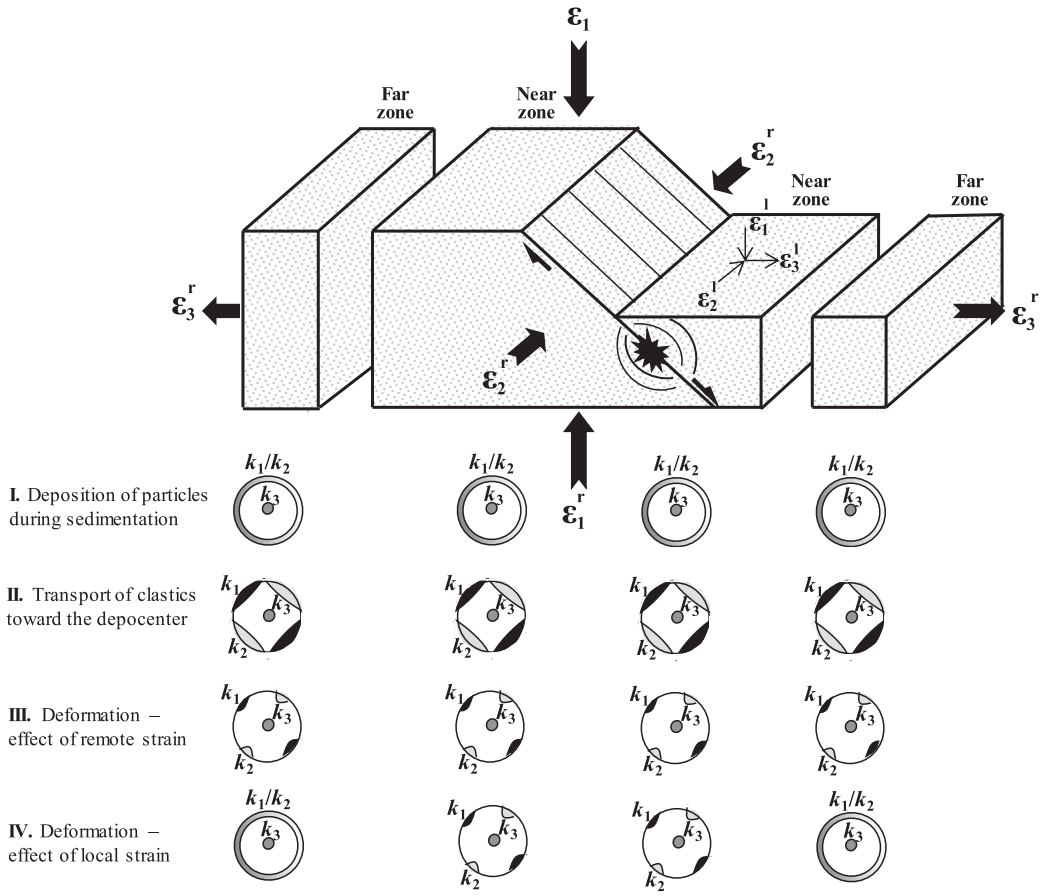

Figure 2. Scheme of faulted blocks and synthetic magnetic fabrics near and far from the fault plane. Four different settings are presented: (I) deposition of particles during sedimentation, (II) transport of clastics towards the depocenetre, (III) effect of remote and (IV) local strain. For each setting the magnetic fabrics are presented as lower-hemisphere of AMS principal axes and their confidence regions. ε_1^r, ε_2^r and ε_3^r are the maximum, intermediate and least principal remote strain axes, respectively. ε_1^l, ε_2^l and ε_3^l are the maximum, intermediate and least principal local (instantaneous) strain axes, respectively. The local strain axes are not necessarily coaxial with the remote strain axes.

two AMS axes overlap on a plane perpendicular to either k_3 or k_1 axes (Fig. 2).

3 GEOLOGICAL SETTING

The Masada Fault Zone (MFZ) comprises a set of normal faults on the western margin of the Dead Sea basin, near Masada, a UNESCO World Heritage Site (Fig. 1). The MFZ is part of the Dead Sea Transform (DST) system, which accommodates ∼105 km of relative sinistral displacement between the African (Sinai) and Arabian plates since the Early-Middle Miocene (Garfunkel 1981, and references therein). The study area is located along a transtentional sector of the DST system (Garfunkel 1981), in which the main strike-slip fault is accompanied by a belt of normal-oblique faults in the western side of the Dead Sea basin (Sagy *et al.* 2003). The soft rocks exposed in the Masada Plain belong to the late Pleistocene Lisan Formation. It consists mostly of lacustrine laminae of aragonite and fine detritus as well as a few gypsum layers, dated between ∼70 000 and 14 000 yr by U-series (Haase-Schramm *et al.* 2004, and references therein). The aragonite precipitated chemically from the upper surface of Lake Lisan whereas the fine detritus, which contains minerals such calcite, dolomite, aragonite, quartz and clay, was carried by annual floods.

The MFZ has repeatedly ruptured the surface (i.e. Lake Lisan bottom) along several kilometers. Studies of the MFZ provide ample examples for fundamental characteristics of earthquakes, such as long-term temporal clustering, repeated faulting on the same planes for a limited time on the order of a few thousands of years, and the formation of subaqueous breccia layers interpreted as seismites (Marco *et al.* 1996; Marco & Agnon 2005). Faults in the MFZ are commonly overlain by continuous horizontal layers, indicating syn-depositional surface ruptures (Fig. 3). Synthetic and antithetic fault planes dip between 40° and 55° and strike between NNW and NNE. All faults show a normal sense of motion (Marco & Agnon 1995) with slip motion predominantly along the dip direction. The strike distribution resembles the basin's large-scale active faults (Sagy *et al.* 2003). The total normal displacement along the faults is up to ∼3.5 m. Based on detailed stratigraphy Marco & Agnon (2005) differentiated several distinct rupture events along individual faults, each of which is between 0.37 and 0.82 m. Paleoseismic records based on breccia layers reveal numerous $M > 6$ earthquake events during the last 70 000 yr (Marco & Agnon 2005).

4 SAMPLING STRATEGY AND METHODS

4.1 Magnetic methods

The AMS was examined along undeformed sedimentary layers (i.e. breccia, fractures or folds were not observed by naked eyes) near

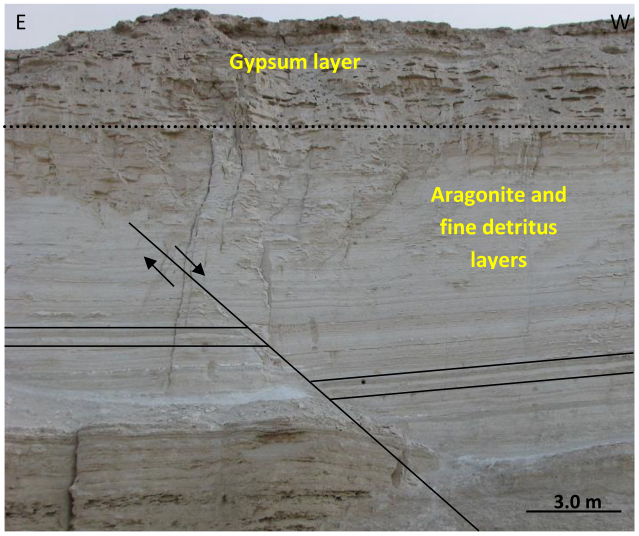

Figure 3. Photograph of a syndepositional, antithetic, normal fault (Fault MM) in the Lisan Formation, Masada Plain, Israel.

three well-documented normal faults in the MFZ (fault numbers 1, 3 and 25 in Marco & Agnon 2005, denoted in this study MM, MP and MS, respectively; Figs 1c and 3). In addition to AMS, the anisotropy of anhysteretic remanent magnetization (AARM) was examined up to ~1 m away from the plane of Fault MS. 162 samples were collected from outcrops within several meters of the three faults studied and 30 samples from two undeformed sedimentary reference outcrops located in the Ami'az Plain, 25 km south of the MFZ (Fig. 1). For sampling we used oriented plastic cubes (2 cm × 2 cm × 2 cm) and cylinders (height and diameter of 2.5 cm) with a negligible diamagnetic AMS signal (-3×10^{-6} SI) that was subtracted later from the measurements. We sampled along the fault planes up to ~1 m intensively at 50 mm increments and further up to ~5.5 m away from the fault planes, at 0.5 m increments.

The AMS and the AARM were studied at the Geological Survey of Israel rock-magnetic laboratory. The AMS was measured with a *KLY-4S* Kappabridge (AGICO Inc., Brno, Czech Republic) and the AARM with AF demagnetizer/magnetizer LDA-3/AMU-1 and a JR-6 spinner magnetometer (AGICO Inc., Brno, Czech Republic). First, the samples demagnetized at a peak field of 100 mT, in which the magnetization values decreased by 90 per cent. Then, the remanent magnetization was imparted in six pairs of antiparallel directions with a DC field of 500 μT and AC field of 50 mT.

The principal susceptibility axes with their 95 per cent confidence ellipses (Jelinek 1978) and bootstrapped confidence limits (Tauxe *et al.* 1991) were analyzed with *Anisoft42* and *Pmag.py* software (http://magician.ucsd/Software/PmagPy), respectively.

To evaluate the magnetic fabrics and to test the possibility that they are associated with inelastic strain in soft rocks close to fault planes, we calculated various anisotropy parameters: the mean magnetic susceptibility, $k_m = (k_1+k_2+k_3)/3$ (Nagata 1961), the lineation, $L = k_1/k_2$ (Balsley & Buddington 1960), the foliation, $F = k_2/k_3$ (Stacey 1960), and the shape of the AMS ellipsoid, T (Jelinek 1981). The latter variable varies from prolate, where $-1 \leq T \leq 0$, to oblate, where $0 \leq T \leq 1$. To test the possibility that different magnetic fabrics are associated with different sedimentary conditions (e.g. Taira 1989), we calculated (1) the anisotropy quotient, $q = (k_1 - k_2)/[(k_1 + k_2)/2 - k_3]$ (Rees 1966), which represents the relative strengths of magnetic lineation and foliation and (2) the imbrication angle, $\beta = 90 - I(k_3)$, where I stands for the inclination of k_3 (Taira 1989). We used *Faultkinwin* 1.2.2 software (Allmendinger 2001) in order to calculate the (instantaneous) strain axes that are associated with the fault-plane solutions of the studied faults.

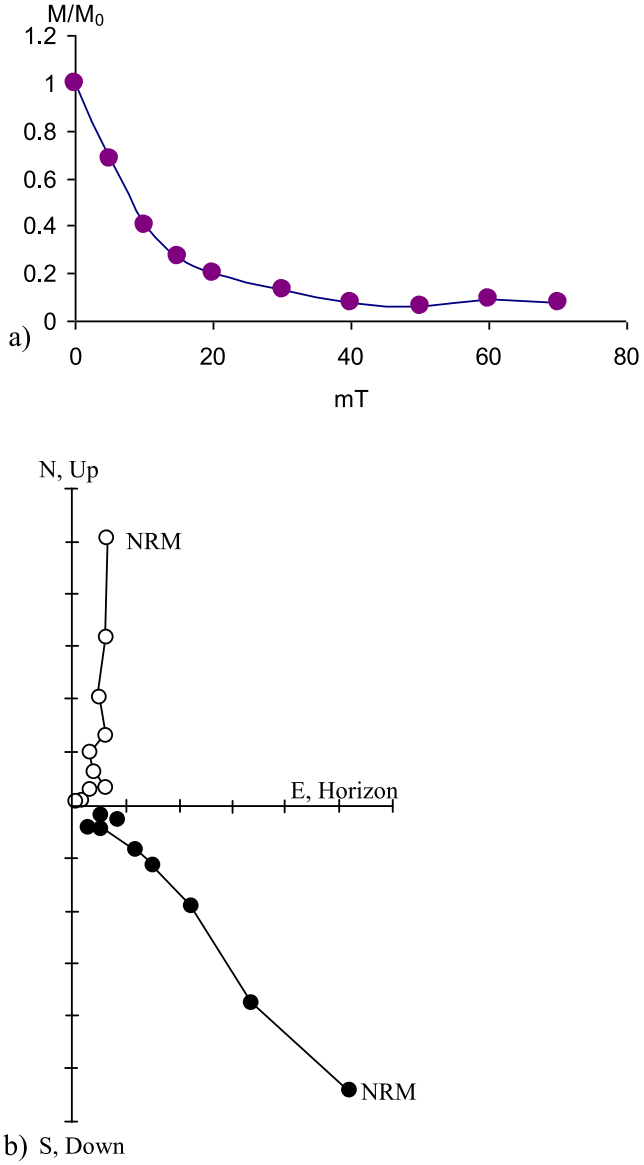

Figure 4. Stepwise alternating field (AF) demagnetization of a representative sample (MS6). (a) Normalized intensity plot of demagnetization experiments. (b) Orthogonal projection of the natural remanent magnetization (NRM) and the characteristics remanent magnetization (ChRM). Solid symbols, plotted on a vertical plane, denote the inclination; open symbols, plotted on an east–west oriented horizontal plane, denote the declination.

Several rock-magnetic experiments were carried out on selected samples in order to characterize the magnetic carriers and their contribution to the magnetic susceptibility and fabrics. Samples were stepwise demagnetized to peak AF of 70 mT, in 5 mT or 10 mT increments. Temperature-dependence susceptibility curves (k–T) were performed, combining the KLY-3S kappabridge with CS-L (low temperature cryostat apparatus between 78 and 273 K) and CS-3 furnace (temperature range between ~25 and 700 °C; AGICO Inc., Brno, Czech Republic).

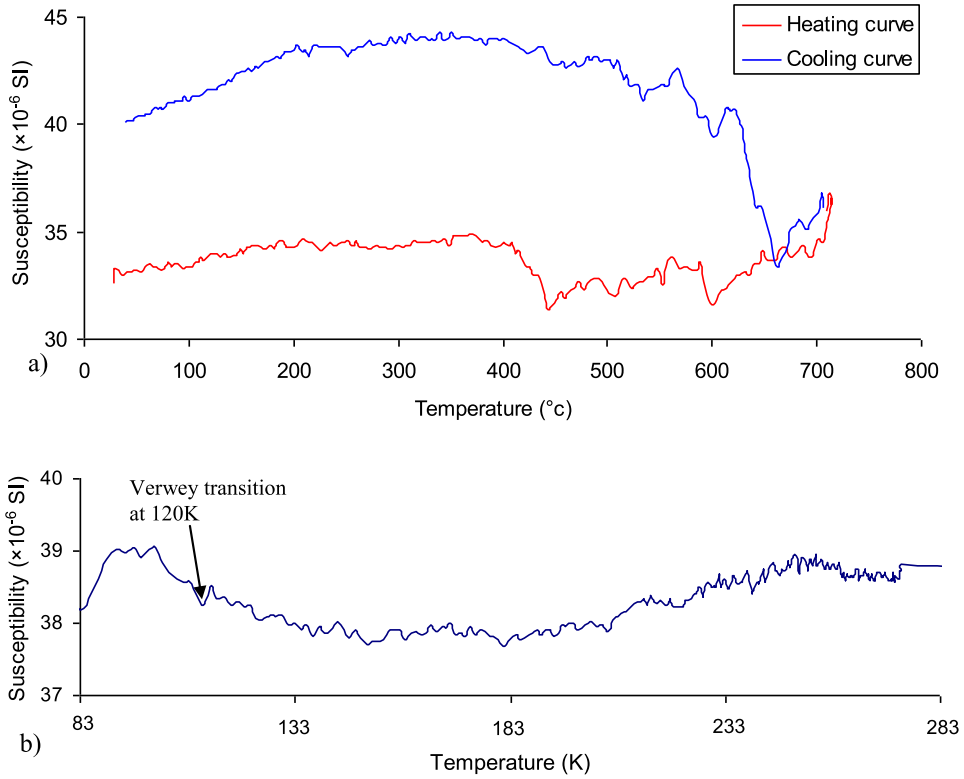

Figure 5. Thermomagnetic (*k–T*) curves of a representative sample (MS15). (a) High-temperature curves (heating and cooling). (b) Low-temperature curve. See text for an interpretation.

Table 2. AMS data of sub-groups in sites MM, MP and MS.

Site	*N*	k_m[a]	*L*[a]	*P′*[a]	*T*[a]	*β*	*q*	*D,I* (k_3)	*D,I* (k_1)
MM(a)	10	28(3)	1.009 (0.009)	1.04(0.01)	0.6(0.3)	18	0.25	113, 81	247, 07
MM(b)	9	36(5)	1.005(0.003)	1.043(0.004)	0.76(0.005)	8	0.13	334, 82	179, 07
MM(c)	12	27(4)	1.007(0.006)	1.038(0.007)	0.67(0.2)	15	0.17	128, 75	290, 15
MM(d)	13	29(3)	1.005(0.003)	1.033(0.006)	0.69(0.18)	11	0.12	107, 80	333, 07
MM(e)	13	27(2)	1.006(0.003)	1.039(0.003)	0.68(0.18)	13	0.19	096, 77	248, 12
MM(f)	5	45(5)	1.005(.003)	1.031(0.003)	0.65(0.19)	5	0.22	109, 85	269, 05
MM(g)	7	47(18)	1.007(0.007)	1.04(0.012)	0.67(0.2)	12	0.13	094, 78	249, 11
MP(a)	8	37(4)	1.004(0.002)	1.036(0.003)	0.77(0.09)	4	0.11	133, 87	004, 02
MP(b)	6	42(8)	1.004(0.002)	1.037(0.004)	0.76(0.09)	2	0.11	042, 88	207, 02
MP(c)	17	49 (9)	1.005 (0.003)	1.036(0.004)	0.75(0.14)	4	0.16	348, 88	126, 02
MP(d)	11	36(3)	1.005(0.002)	1.039(0.005)	0.74(0.09)	4	0.17	162, 86	007, 04
MS(a)	9	30(9)	1.008(0.003)	1.038(0.005)	0.55 (0.09)	7	0.27	069, 83	248, 07
MS(b)	13	3 2(9)	1.00 5(0.002)	1.0 42(0.004)	0. 748(0.1)	6	0.16	065, 83	244, 07
Reference-aragonite (A)	20	48(12)	1.002(0.001)	1.026(0.003)	0.87(0.06)	3	0.07	280, 87	149, 02
Reference-detritus (B)	10	76(14)	1.003(0.001)	1.016(0.007)	0.48(0.36)	6	0.19	279, 84	160, 03

Notes: N, number of specimens; k_m, mean susceptibility, (in 10^{-6} SI units) *L*, lineation; *P′*, corrected anisotropy degree (not referred to in the text); *T*, shape of the AMS ellipsoid, *β*, imbrication angle; *q*, anisotropy quotient;
D,I(k_3), declination and inclination of the minimum susceptibility axis (geographic coordinates); *D,I*(k_1), declination and inclination of the maximum susceptibility axis (geographic coordinates).
[a]Standard deviation in parentheses.

4.2 Geochemical methods

To test the possible effect of Fe and Mn ions on the magnetic fabrics we analysed the bulk mineralogy of 13 samples using X-ray diffraction (XRD) and the chemical composition of their $CaCO_3$ fraction at the Geological Survey of Israel. Since the carbonate fraction (laminae of aragonite) is significantly more sensitive to diagenetic processes than the fine detritus, the $CaCO_3$ fraction of these samples was extracted as follows: 0.5 g of sample was treated with 15 ml of 3M HNO3 for 1 hr. The solution was separated and analysed for major elements including Fe and Mn ions using an Inductively Coupled Plasma Mass Spectrometer (ICP- AES; Perkin Elmer OPTIMA 3300; $1\sigma < 3$ per cent).

5 ROCK MAGNETISM OF THE LISAN FORMATION

AF experiments indicate that the ferromagnetic carriers have low coercivity spectra. The characteristic remanent magnetization (ChRM) of the rocks shows the expected late Pleistocene direc-

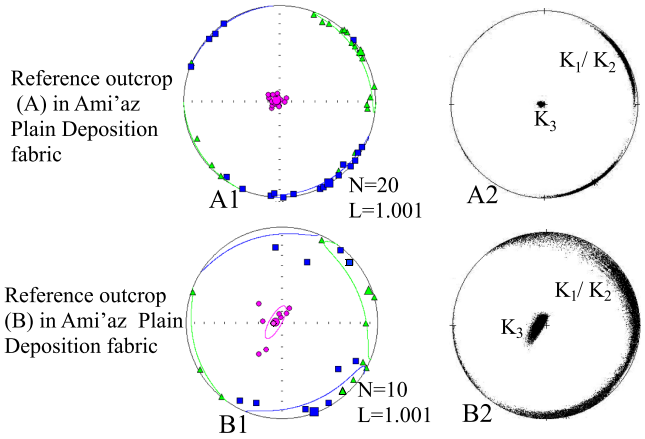

Figure 6. Magnetic fabrics detected in the Ami'az Plain (A1, B1). A1–B1: Lower-hemisphere, equal-area projection of AMS principal axes and the 95 per cent confidence ellipses; Blue squares, green triangles and pink circles represent k_1, k_2 and k_3 axes, respectively. A2–B2: Lower- hemisphere, equal-area projection of AMS principal axes and the bootstrapped confidence limits.

tion (Fig. 4). High-temperature k–T curves show a significant decrease at ∼440 and ∼580 °C during heating and significant increase at ∼620, ∼580 and ∼440 °C during cooling (Fig. 5a), corresponding to the presence of titanomagetite and probably to formation of magnetite and hematite due to phase transitions during heating. Yet, in the low-temperature, the k–T curves show defined Verwey transition near 120 K implying to magnetite. If some greigite is present, then there is a good chance that inherited magnetite where altered or dissolved (e.g. Roberts *et al.* 2011).

The Hysteresis behaviour and rock-magnetic properties of the aragonite and detrital lamina of the Lisan Formation were intensively studied by Marco *et al.* (1998), Ron *et al.* (2006), Levi *et al.* (2006a) and Nowaczyk (2011). Based on these studies the aragonite layers are mostly diamagnetic, and titanomagnetite is the main ferromagnetic carrier in the detrital layers. The hysteresis parameters indicate that the titanomagnetite grains are pseudo-single domain (PSD) to strong multidomain (MD) size and are found in detrital and even aragonite layers that are mostly characterized by diamagnetic behaviour (figs 5–7 in Ron *et al.* 2006). Marco *et al.* (1998) suggested based on the AF experiments, SEM and microprobe data that the Lisan layers contain particles of the titanomagnetite series. The AF coercivity, the unblocking temperature spectra, and the saturation of IRM at 300 mT also suggest titanomagnetite composition, predominantly of PSD grain size with some MD and SPM grains (Supplementary Data item I).

6 MAGNETIC FABRICS

The values of k_m in Masada Plain fall in a narrow range between 30 and 50 $\times 10^{-6}$ SI (Table 2), which is typical for soft clay-carbonate sediments (e.g. Cifelli *et al.* 2004; Levi *et al.* 2006b). k_m values of samples that were taken close to and away from the fault planes are indistinguishable (Table 2).

The AMS of the reference outcrops in the Ami'az Plain is characterized by large 95 per cent confidence ellipses (Figs 6A1 and B1) and by overlap of the bootstrapped confidence limits (Fig. 6B2) of k_1 and k_2 axes. The AMS fabrics next to Fault MM are shown in Fig. 7. At ranges of 70–255 cm (hanging wall) and 65–550 cm (footwall) from the fault planes k_3 axes are subvertical and well grouped, whereas the 95 per cent confidence ellipses and the bootstrapped confidence limits of the subhorizontal k_1 and k_2 axes overlap. On the other hand, close to Fault MM, at ranges of 0–50 cm (hanging wall) and 0–55 cm (footwall) from the fault planes, the AMS fabrics are characterized by well-grouped and isolated k_1, k_2 and k_3 axes. Within the area enclosed between two fault strands (intermediate block, zone II in Fig. 7), the AMS also shows similar fabric characteristics. Likewise, results obtained close to faults MS and MP show well grouped and isolated k_1, k_2 and k_3 axes next to fault strands, and overlapping k_1 and k_2 axes away from these strands (Figs 8 and 9).

In three out of five AMS stereograms ranging up to 55 cm, k_2 axes align with the strike of Fault MM (Fig. 7; Stereograms I.2, I.3 and II.1). In the other stereograms (Fig. 7, III.1, III.2), either k_1 or k_2 axes are oblique to the strike of the fault. Likewise, either k_1 (Fig. 8, I.2, II.1 and II.2) or k_2 axes (Fig. 9, I.1, I.2) are parallel to the strikes of faults MP and MS, respectively. In four out of five AMS stereograms of Fault MM the AMS axes (Fig. 7; Stereograms I.2, I.3, II.1 and III.1) are compatible with the fault-plane solutions (Fig. 7d). In the other stereogram (Fig. 7, III.2), k_1 and k_2 axes are switched. Likewise, the AMS stereograms of faults MP and MS are compatible with the fault-plane solutions, while in Fault MP k_1 and k_2 axes are switched (Fig. 8). The AARM fabric next to Fault MS (site I.1) shows subvertical, well-grouped k_3 axes and subhorizontal k_1 and k_2 axes with overlapping 95 per cent confidence ellipses and bootstrapped confidence limits (Fig. 10).

Fig. 11 shows the high values (>1.015) of the magnetic lineation L near Fault MM relative to L values from the reference outcrops in the Ami'az Plain (∼1.0025). A similar pattern is seen in the hanging wall, although the values are lower than those of the footwall. There are only small differences in T values between sites that have well-grouped AMS axes and those that have subhorizontal k_1 and k_2 axes with relatively large 95 per cent confidence ellipses (Table 2; Supplementary Data item II). However, on q–β plot (Fig. 12) that typically indicates a transition from one sedimentary environment to another (i.e. from gravity sedimentation to current conditions; Taira 1989) samples that have a well-grouped AMS axes cannot be separated from samples that have subhorizontal k_1 and k_2 axes with relatively large 95 per cent confidence ellipses.

7 GEOCHEMICAL RESULTS

XRD results show that all samples consist of aragonite as the most dominant (>50 per cent) mineral, with some minor (∼5–20 per cent) quartz, phyllosilicates and calcite, as well as traces (<5 per cent) of gypsum, dolomite and halite (Supplementary Data item III, Table 1).

The average contents of Fe and Mn of the 13 representative samples are 1777 and 89 ppm, respectively (Table 3). Fig. 13 shows that the distribution of major elements between sets of samples that were taken close to and away from the fault planes is almost indistinguishable.

8 DISCUSSION

The AMS fabrics of the reference Lisan outcrops in the Ami'az Plain (Fig. 6, fabrics A1; B1) fit well with the criteria defining sedimentary processes (*settings* 1 and 2 in Table 1) and, hence, can be termed 'deposition fabrics'. The AMS fabrics obtained meters away from the fault planes in the Masada Plain (Fig. 7, fabrics, I.1, III.3; and Fig. 8, fabrics, I.1, II.2) also fit well with the criteria defining sedimentary processes (Supplementary Data item II). The

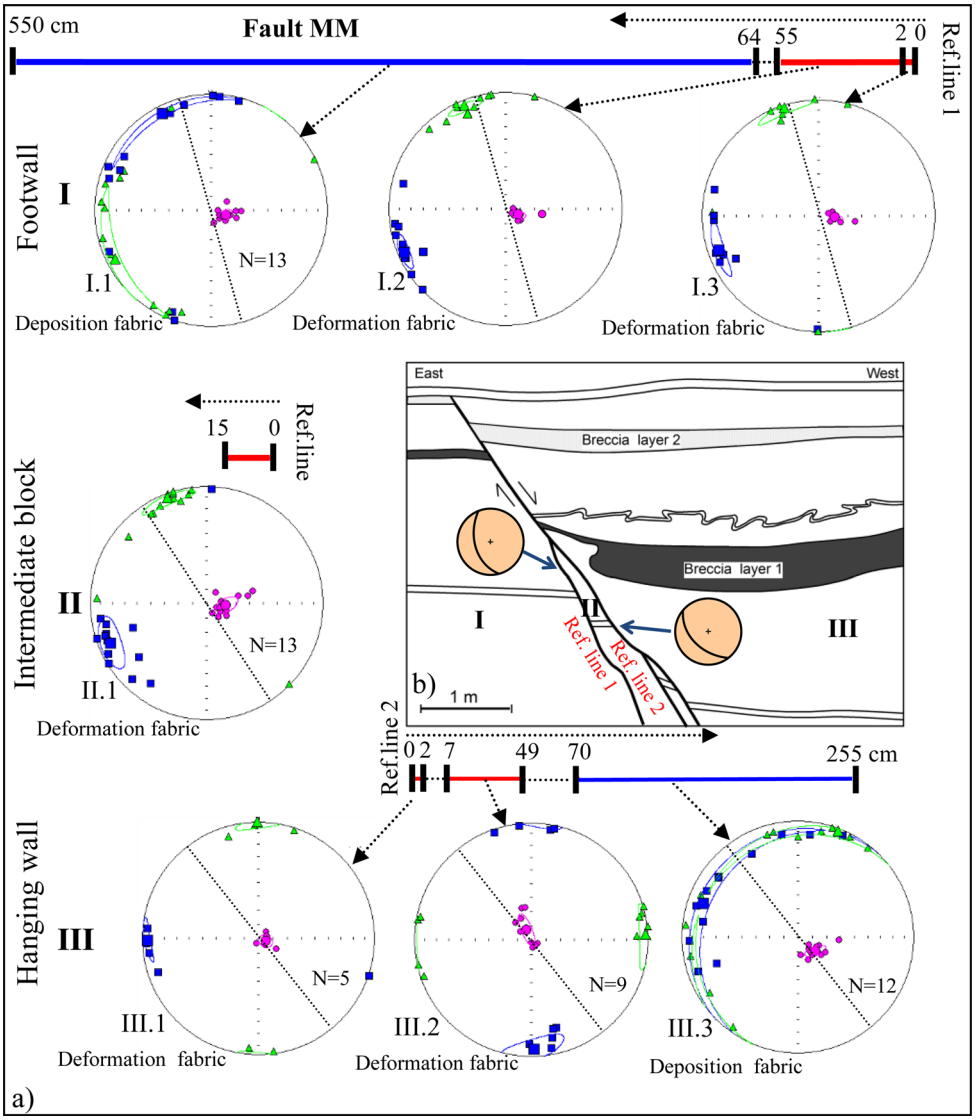

Figure 7. Magnetic fabrics detected at Fault MM, Masada Plain. (a) Magnetic fabrics detected at the footwall (I), intermediate block (II) and hanging wall (III) of the fault. Blue squares, green triangles and pink circles represent k_1, k_2 and k_3 AMS axes. Blue and red lines mark zones in which either deposition fabric or deformation fabric is detected, respectively. The magnetic fabrics are presented in lower-hemisphere equal-area projections of principal AMS axes and their 95 per cent confidence regions. Dashed lines indicate the strike direction of the nearby fault strand. The distance from fault strands (reference lines 1 and 2) are marked in centimetres. (b) Sketch of Fault MM after Marco & Agnon (2005), in which line drawings are traced from photographs (Fig. 3), emphasizing bedding, breccia layers (pattern) and fault planes (solid lines). Two small stereograms show the orientations of the fault strands. Footwall (I), intermediate block (II) and hanging wall (III) are indicated. (c) Lower-hemisphere, equal-area projection of AMS principal axes and the bootstrapped confidence limits. (d) Two fault-planes and moment-tensor solutions calculated for the footwall (I), and hanging wall (II). Dashed arrows mark the dip-slip direction. ε_1^1, ε_2^1 and ε_3^1 are the instantaneous maximum, intermediate and least principal strain axes, respectively.

AMS fabrics of Lisan layers next to (<0.5 m) fault planes are characterized by well-grouped k_1 and k_2 axes, and, hence, meet the criteria of deformation processes (*settings* 3 and 4; Fig. 7, I.2, I.3, II.1, III.1 and III.2; Fig. 8, I.2, II.1; Fig. 9, I.2). Following, we first demonstrate the relation of the obtained AMS fabrics to deformation processes. Next, we discuss the possibility that these AMS fabrics were formed under *setting* 4 and are compatible with the hypothesis that distinguish AMS fabrics were formed due to fault-driven local strain field.

The possibility that the AMS fabrics next to the faults were formed due to transport of clastics (*setting* 2) into Lake Lisan is excluded for four main reasons:

(1) The AARM fabric of samples close to Fault MS unmistakably shows 'deposition fabrics' (scattered k_1 and k_2 axes along the girdle; see Fig. 10), while the AMS fabric of the same samples shows well-grouped k_1 and k_2 axes (Fig. 9, I.2). Rock-magnetic experiments demonstrate that the dominant ferromagnetic phase of the Lisan Formation is titanomagnetite grains of PSD to strong MD (Marco *et al.* 1998; Levi *et al.* 2006b). The state of the titanomagnetite domain might play an important role in the acquisition of AMS fabrics. For MD grains the magnetization has maximum susceptibility values in the direction of the grains' long axis ('normal' fabric), while in SD grains an 'inverse' fabric with maximum susceptibility in the direction of the grains' short axis may occur (Rochette *et al.* 1992; Borradaile & Jackson 2004 and references therein). Hence, if the

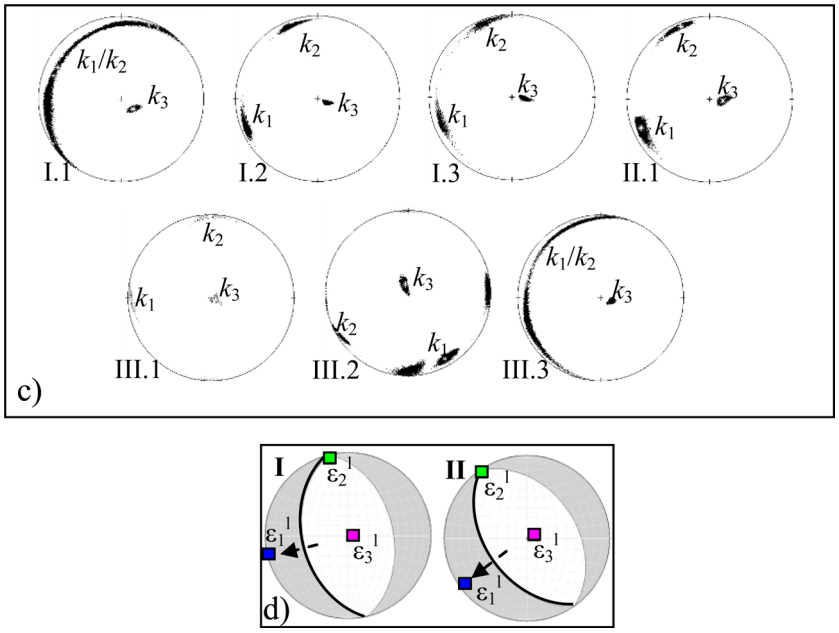

Figure 7. (*Continued*)

titanomagnetite contributes somewhat to the magnetic fabrics of the studied Lisan Formation, 'normal' AMS fabrics are expected.

We suggest that these grains preserve the original 'deposition fabrics' as revealed by the AARM fabric, and that this fabric was not affected by the faulting processes. Therefore, it is suggested that the AMS fabrics of the aragonite layers are controlled by the alignment of aragonite needles (Ron *et al.* 2006), which are the most common diamagnetic mineral in the Lisan Formation, and probably by alignment of sporadic paramagnetic minerals in the detritus layers.

(2) The AMS fabric varies away from the fault planes on a scale of centimetres. It is unlikely that settling of particles and transport of clastics under sedimentary conditions (*settings* 1 and 2) could have changed the fabrics on such a small scale; (3) Differences in q and β values usually indicate transitions from one sedimentary environment to another. Fig. 12 shows clearly that samples with well-grouped AMS axes cannot be separated from samples that have subhorizontal k_1 and k_2 axes with relatively large 95 per cent confidence ellipses and bootstrapped confidence limits (Supplementary Data item II). This suggests that the formation of the two types of magnetic fabrics is not related to different sedimentary environments and conditions and (4) Under sedimentary conditions that involve transport of clastics eastward towards the Dead Sea depocentre (Alsop & Marco 2012), k_1 axes should be parallel to the transport direction and be aligned along an east–west axis over the entire region. However, the present results indicate that k_1 axes next to faults MP and MS are perpendicular to the strikes of the faults (trending NNE and NW, respectively) and as a result are not aligned along an east-west direction throughout the entire region (Fig. 8, I.2, II.1; Fig. 9, I.2). In Fault MM (Fig. 7, I.2, I.3, II.1 and III.1) k_1 axes are aligned along ~ENE–WSW direction, but this seems to be due to the perpendicular relation between k_1 axes and the fault plane, as in faults MP and MS.

There are several arguments that clearly indicate that fluid circulation did not play a significant role in the formation of the unique magnetic fabrics near the fault planes:

(1) Aragonite is an unstable mineral that in the presence of meteoric water changes to calcite (Katz *et al.* 1972). The bulk mineralogy of selected samples shows dominancy of aragonite and the lack of significant amount of calcite. This indicates that fluids were hardly passed through the sediment and along the fault planes after deposition. Aragonite has a very distinct Ca^{2+}/Sr^{2+} ratio, which is ten times greater then that of calcite. The results of the ICP-AES show that the Ca^{2+}/Sr^{2+} ratio remains constant for all samples (Table 3, Supplementary Data item IV), indicating that the contribution of calcite due to transformation of aragonite into calcite is negligible. This is in agreement with the results of the XRD measurements, indicating the predominance of aragonite in all samples (Supplementary Data item III, Table 1).

(2) The colour of the fine laminae of aragonite in the Lisan Formation is purely white. If indeed, fluids containing dissolved magnetic minerals (Fe and Mn) played a role, then these laminae near the fault planes would have stained by yellow to reddish colours. Though this effect has been documented near opening-mode fractures elsewhere in Amiaz Plain, it was not observed next to faults in Masada Plain.

(3) Differences in k_m values may indicate differences in the content of magnetic minerals. The present results indicate that there are no significant differences in k_m values between sets of samples that show 'deformation fabrics' close to fault planes and those show 'deposition fabrics' away from the fault planes (Supplementary Data item V).

(4) High concentrations of Fe^{2+} and Mn^{2+} close to fault planes may be the results of fluids circulating along the fault planes. In such a case, Fe^{2+}/Mn^{2+} ratio is expected to be constant and similar to the source fluid (Table 3 and Fig. 14). The present results indicate that there are no significant differences in the distribution of major elements (Ca^{2+}, Sr^{2+}, Mg^{2+}, Al^{2+}, Mn^{2+} and Fe^{2+}) between sets of samples showing 'deformation fabrics' close to fault planes and those showing 'deposition fabrics' away from the fault planes (Table 3 and Fig. 13). Moreover, the results of the ICP-AES show that there is no correlation between Mn and Fe contents for samples that were taken close to fault planes (Fig. 14). Hence, the potential

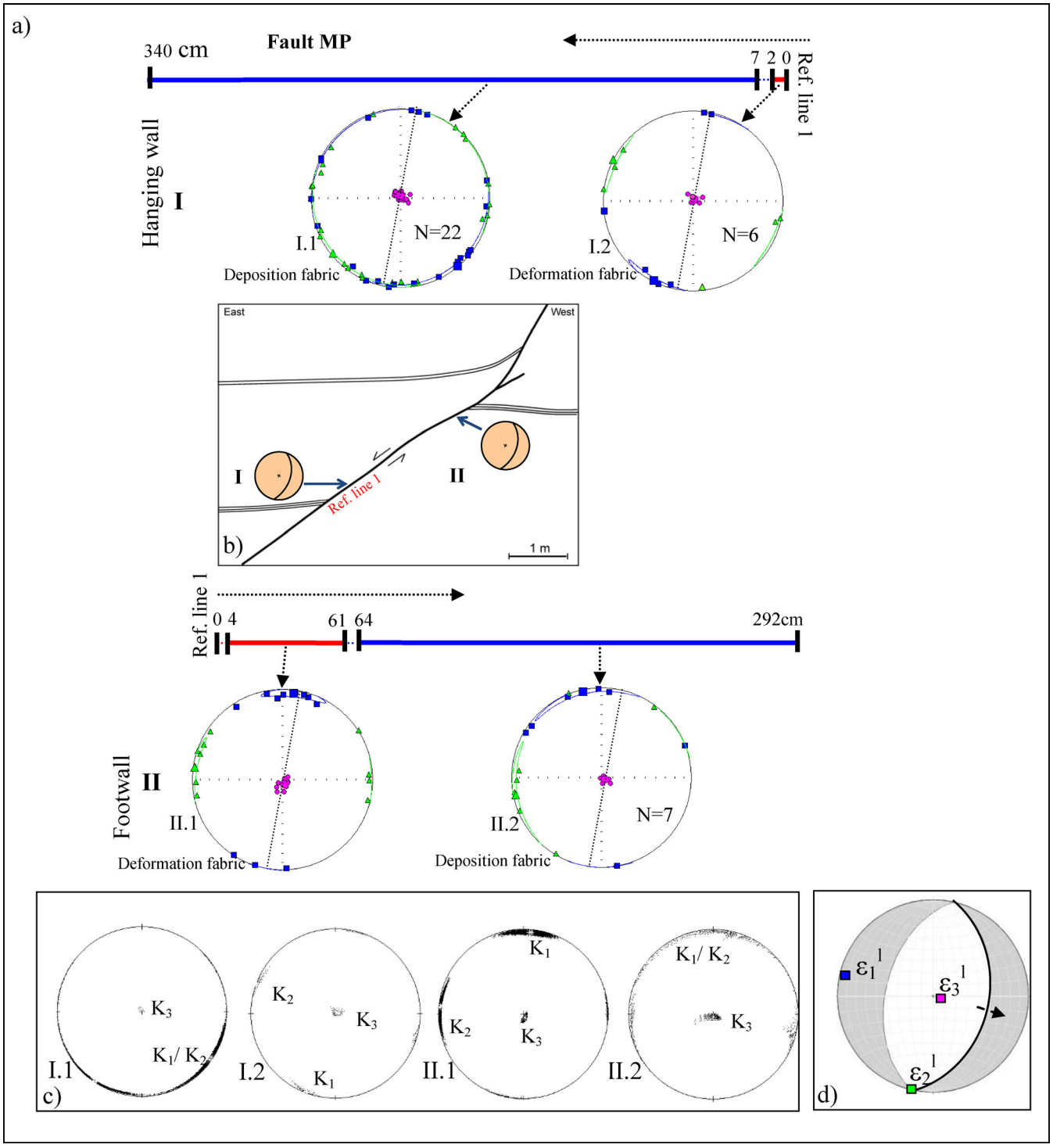

Figure 8. Magnetic fabrics detected at Fault MP, Masada Plain. For legend see Figure MM. (a) Magnetic fabrics detected at the hanging wall (I), and footwall (II) of the fault. (b) Sketch of Fault MP, in which line drawings are traced from photographs, emphasizing bedding, breccia layers (pattern), and fault planes (solid lines). Two small stereograms show the orientations of the fault strands. Hanging wall (I), and footwall (II) are indicated. (c) Lower-hemisphere, equal-area projection of AMS principal axes and the bootstrapped confidence limits. (d) A fault-plane and moment-tensor solution calculated for the footwall (I). Dashed arrows mark the dip-slip direction. ε_1^1, ε_2^1 and ε_3^1 are the instantaneous maximum, intermediate and least principal strain axes, respectively.

effect of fluid circulation on the observed unique magnetic fabrics near the fault planes can be excluded.

The AMS fabrics reflect the inelastic strain that was stored in the soft rocks within decimeters of the three faults studied during the deformation process. We therefore interpret the AMS fabrics next to the faults as 'deformation fabrics' and suggest that they provide evidence for the inelastic strain stored in the soft rocks during faulting events along and close to the fault planes. The evidence that supports the possibility that this inelastic strain is an

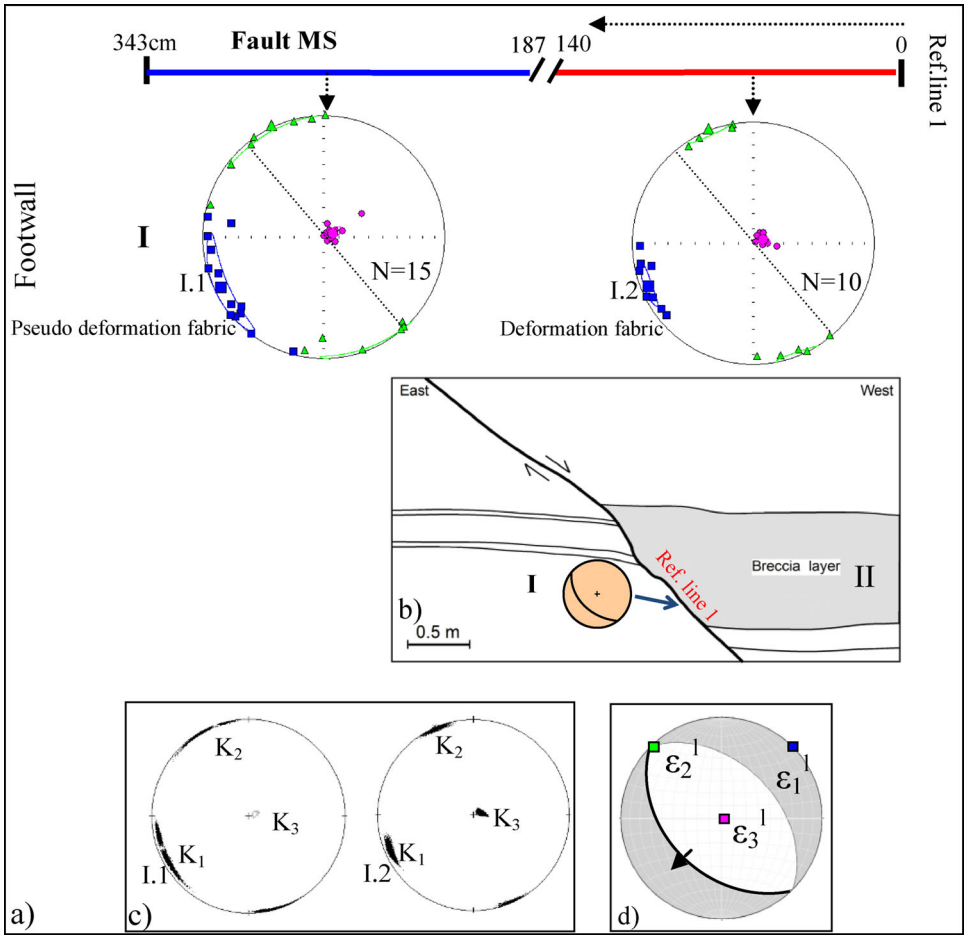

Figure 9. Magnetic fabrics detected at Fault MS, Masada Plain. For legend see Figure MM. (a) Magnetic fabrics detected at the footwall (I) of the fault. (b) Sketch of Fault MS, in which line drawings are traced from photographs, emphasizing bedding, breccia layers (pattern) and fault planes (solid lines). A small stereogram shows the orientation of the fault strand. Footwall (I) and hanging wall (II) are indicated. (c) Lower- hemisphere, equal-area projection of AMS principal axes and the bootstrapped confidence limits. (d) A fault-plane and moment-tensor solution calculated for the footwall (I). Dashed arrows mark the dip-slip direction. ε_1^1, ε_2^1 and ε_3^1 are the instantaneous maximum, intermediate and least principal strain axes, respectively.

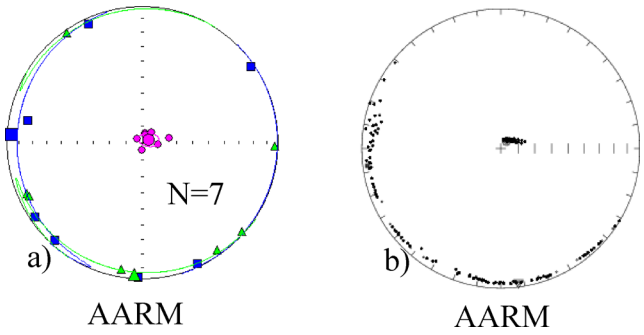

Figure 10. Anisotropy of Anhysteretic Remanent Magnetization (AARM) measurements of representative samples taken near Fault MS (site-I.1). (a) Lower-hemisphere, equal-area projection of AARM principal axes and the 95 per cent confidence ellipses; Blue squares, green triangles and pink circles represent k_1, k_2 and k_3 axes, respectively. The 95 per cent confidence ellipses of k_1 and k_2 is about 50° which is characterizing 'deposition fabrics' (see also, Supplementary Data item II). (b) Lower-hemisphere, equal-area projection of AARM principal axes and the bootstrapped confidence limits.

expression of a released, faulting-induced local strain field (*setting* 4) and is not an expression of the long-term remote strain field are:

(1) 'Deformation fabrics' detected only close (<0.5 m) to the fault planes; (2) Either k_1 or k_2 axes parallel to the fault strikes (Figs 7–9); (3) L values showing relatively high values next to the fault planes and sharply dropping to the background values of 'deposition fabrics' at a distance of ∼1 m from the fault planes (Table 2 and Fig. 11); (4) k_1 and k_2 axes occasionally switched next to the fault planes and (5) In four cases (Fig. 7, II.1, III.2; Fig. 8, I.2, II.1) neither k_1 nor k_2 axes are compatible with the expected DST-related remote stress field (Table 1; Eyal 1996). This non-uniformity of the stress field and only sporadic compatibility of the AMS and remote strain axes (Fig. 7, I.2, I.3; Fig. 9, I.2) over an area of a few square kilometres are best interpreted as an effect of local rather than remote stress field.

The 'deformation fabrics' may be the expression of two different modes of local strain field: (1) Static strain field accumulating near the fault plane, usually due to the long-term steady plate motions. The static strain field is commonly explained by the 'elastic rebound theory' or the 'quasi-static damage theory' (e.g. Dugdale 1960; Turcotte & Schubert 1985; Cowie & Scholz 1992; Scholz 2002) and (2) dynamic strain field that formed near the fault plane due to fast radiation of the acoustic waves (e.g. Shearer 1999) and fast rupture propagation (e.g. Ben-Zion & Shi 2005; Rice *et al.* 2005; Lyakhovsky & Ben-Zion 2008; Ma & Andrews 2010).

Based on the rheology of the soft Lisan host rock and the setting of the syndepositional faults studied, it is likely that the effect of the static strain (stress) next to the faults was minor and the dynamic

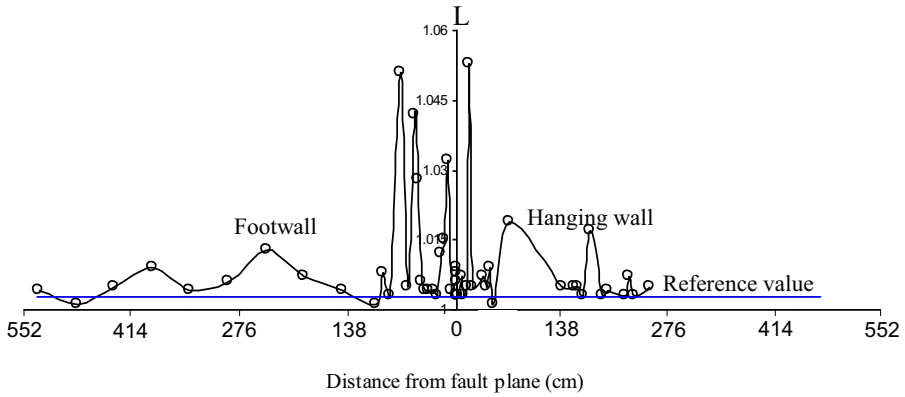

Figure 11. Variations of the L values with the distance from Fault MM. Footwall and hanging wall are indicated. Blue horizontal line represents the average L values of the reference site in the Ami'az Plain.

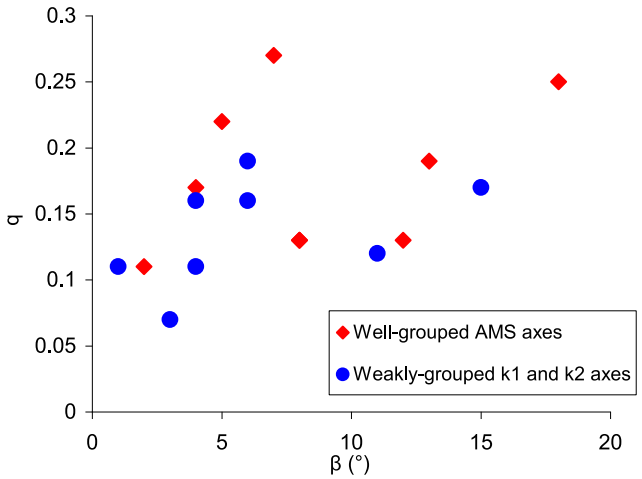

Figure 12. q (lineation intensity) versus β (imbrication angle) values of the AMS measurements, Masada Plain. The fabrics that have well-grouped AMS axes (red circles) cannot be differentiated from fabrics whose k_1 and k_2 axes are weakly grouped (blue squares).

strain (stress) was dominant. First, the total displacement along Fault MM is the result of three dynamically-induced earthquake events, as demonstrated by the associated breccia layers (Marco & Agnon 2005). Second, a static strain field commonly accumulates due to frictional forces that lock the steady motion of the blocks on either side of the fault. Under the Lake Lisan water column, the calculated static frictional forces of the studied faults are very low (Supplementary Data item VI) and, consequently, the static strains along them are negligible. Third, static strains near the surface are low and would not modify the 'deposition fabrics' to 'deformation fabrics' without additional strains. This conclusion is supported by the detection of the depositional magnetic fabric away from the fault planes. Fourth, during dynamic rupturing/faulting, the local strain field varies significantly through the damage zone (Ma & Andrews 2010, fig. 14).

In inelastic dynamic models, in which slip rate, rock mechanical properties, depth, seismic wave velocities and remote stresses were taken into account, the near-surface inelastic strain is induced by the seismic waves ahead of the rupture front. The simulations show that the compressive and the extensive stresses (i.e. analogue to k_3 and to k_1 axes, respectively) are changeable around the fault, arising from variations over time of the seismic waves that interact with the small confining pressure near the surface. As the cohesion decreases upward, the inelastic zone (i.e. damage zone) broadens towards the surface. Likewise, in the 'deformation fabrics' either k_2 or k_1 axes are parallel to the strikes of the faults, implying that the strain field was interrelated with the rupture propagation, and, hence, was dynamic. Noticeably, in normal faulting the intermediate shortening axis (ε_2) is parallel to the strike of the fault and the maximum

Table 3. Chemical contents in ppm or % and ratios.

Sample	Ca	Sr	Mg	Al	Mn	Fe	%Ca	%$CaCO_3$	%SiO_2	Ca/Mg	Fe/Mn	SiO_2/Al_2O_3
MM-4	243613	5350	7594	683	103	1814	24.4	60.8	2988	32.1	17.5	2.3
MM-16	256759	5757	6419	565	102	1489	25.7	64.1	2736	40	14.6	2.6
MM-17	244572	5375	7281	633	90	1669	24.5	61.1	2817	33.6	18.5	2.4
MM-49	231164	5060	7652	591	125	1575	23.1	57.7	2613	30.2	12.6	2.3
MM-65	241627	5121	6807	734	86	2039	24.2	60.3	3107	35.5	23.6	2.2
MM-57	240646	5457	7375	848	116	2018	24.1	60.1	2914	32.6	17.4	1.8
MM-35	252892	5551	6411	559	85	1419	25.3	63.2	2531	39.4	16.7	2.4
Average	243547	5333	7151	641	101	1717	24	60.8	2852	34	17.4	2.4
Std. (1)	9119	274	529	69	15	217	1	4.6	197	4	4	0.1
MP-11	216435	4191	8098	942	87	2081	21.6	54	2837	26.7	24	1.6
MP-26	219045	4447	7065	743	107	1690	21.9	54.7	2809	31	16	2
MP-30	231765	4770	6199	680	83	1513	23.2	57.9	2816	37.4	18	2.2
MP-34	236406	4848	6767	744	78	1822	23.6	59	2933	34.9	23	2.1
MP-45	197288	3896	8367	857	164	2166	19.7	49.3	2738	23.6	13	1.7
MP-47	255832	5457	6676	781	78	1637	25.6	63.9	3129	38.3	21	2.1
Average	225913	4564	7032	777	89	1777	23	56.4	2849	33	20	2
Std. (1)	9684	303	796	114	13	239	1	4.8	57	5	4	0.3

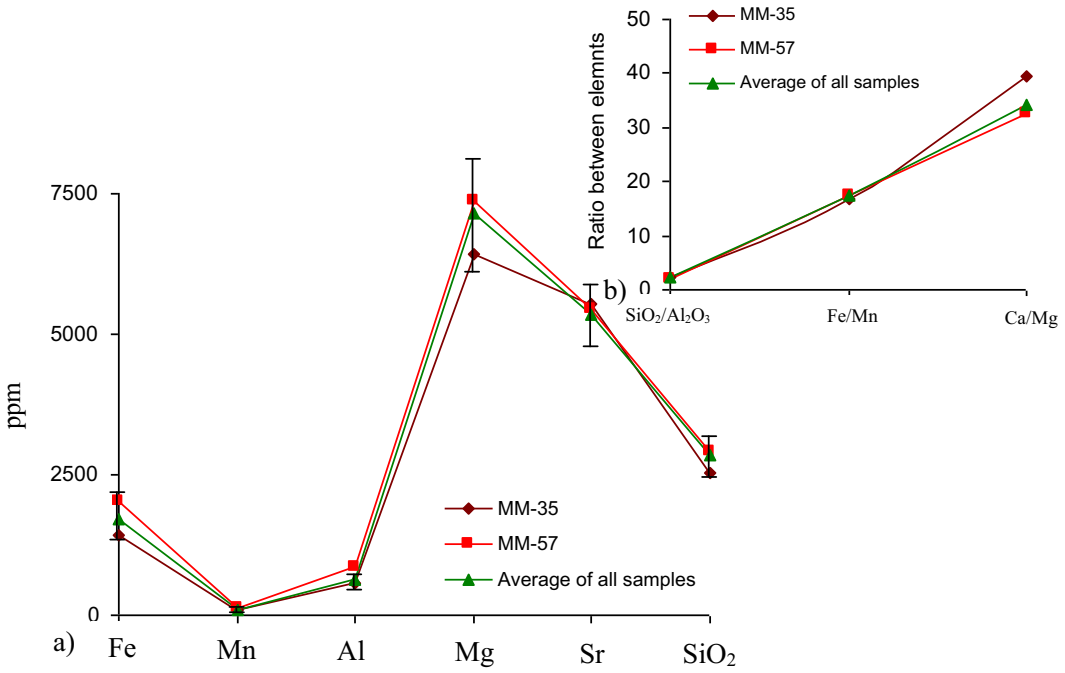

Figure 13. Chemical results of two representative samples that were taken near fault MM. (a) chemical elements (in ppm) of samples MM35 and MM57 marked by brown diamonds and red squares, respectively. Error bars of 2 STD are marked. (b) Chemical composition ratios SiO_2/Al_2O_3, Fe/Mn and Ca/Mg of sample MM35. Green triangle represents the average values of all samples.

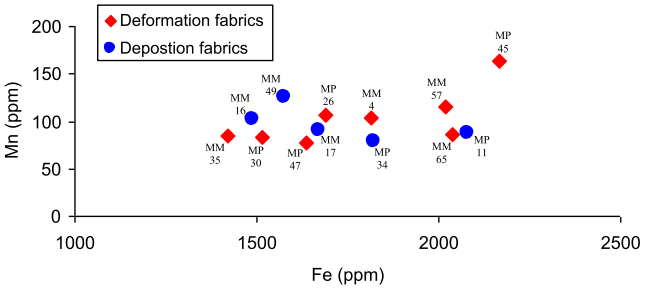

Figure 14. Mn versus Fe contents of 13 selected samples from sites MM and MP. Red diamonds and blue circles indicate 'deformation fabrics' and 'deposition fabrics', respectively.

shortening axis (ε_1) is perpendicular to it (Twiss & Moores 1992). An analogy to this is seen in four stereograms, in which k_2 axes are parallel to the strikes of the faults and k_1 axes are perpendicular to it (Fig. 7, I.2, I.3, II.1; Fig. 9, I.2). Fifth, the width W of the damage zone can be predicted from the total displacement D based on a correlation between the two attributes (e.g. Faulkner *et al.* 2011). In a quasi-static propagation the damage zone becomes wider as the fault displacement advances. Generally, the $W/D_{\text{total}} \geq 1$ for a total displacement of up to ~100 m (Faulkner *et al.* 2011, and references therein). In this mode of formation, the damage zone depends mainly on the fault displacement history (Tveranger *et al.* 2008; Childs *et al.* 2009; Faulkner *et al.* 2010; Torabi & Berg 2011). In dynamic propagation, the size of the damage zone depends mainly on the rupture propagation velocity (Rice *et al.* 2005). In this mode of formation, W could be much narrower than that formed by the quasi-static propagation, and it could be either symmetric or asymmetric around the faults (e.g. Ben-Zion & Shi 2005; Rice *et al.* 2005; Faulkner *et al.* 2011). In this study $W/D_{\text{total}} = \sim 0.2$, indicating that this ratio is comparable to values of dynamic propagation. In addition, the width of the damage zone in Fault MM is symmetric around the fault plane (~0.5 m at the hanging wall and footwall) and in Fault MP is asymmetric (~0.6 and 0.02 m at the hanging wall and footwall, respectively). These observations are best explained by dynamic rather than static strains along the faults. Based on the above arguments, it is plausible to attribute the magnetic fabrics and the associated inelastic deformation to coseismic dynamic faulting.

This study shows that the 'deformation fabrics' were acquired during the rupturing process over a short time and localized space. Hence, they cannot be associated with an extensional (e.g. Cifelli *et al.* 2005) or compressional (Kissel *et al.* 1986) component of the far field.

We envision that during the rupturing event the seismic waves that passed through the Lisan soft rocks facilitated rotation and re-arrangement of aragonite needles in the following manner. Clusters of aragonite needles form an apparent shape, in which its long and short axes are horizontal and vertical, respectively. In this cluster of particles the *c*-axes of the aragonite needles are vertical and parallel to the vertical k_3 axes and to the local maximum shortening axis (ε_1^1). The long axis of the apparent shape is effectively parallel to k_1 axes and to the maximum elongation axes (ε_3^1). Noted, that in this schematic model k_1 axes can be parallel, perpendicular or even oblique to the strike of the fault plane, depending on the orientation of ε_3^1 with respect to the fault plane during the rupturing event. The possibility that paramagnetic particles also involved with the soft-sediment deformation should be further studied in the future.

This study shows that most of the AMS stereograms that reflect a local and inelastic strain field resemble fault-plane solutions (i.e. the principal axes of the AMS and strain ellipsoids are coaxial; Figs 7–9). This conspicuous result indicates that although the local strain field is inelastic, it can provide a first-order approximation for the fault mechanism in the elastic strain regime. Hence, we suggest that the AMS method may be applicable for determining the fault-plane solutions of past earthquakes in soft rocks and could be useful in such rocks where strain markers are invisible.

9 CONCLUSIONS

The present AMS analysis corroborated by field observations and geochemical data demonstrates that the 'deformation fabrics' close to three normal faults in the Dead Sea basin are the product of dynamic faulting events. Variations in the AMS fabrics and magnetic lineations define the size of the inelastic strain field and its shape surrounding the fault planes. The present AMS results show that the damage zone width is crudely similar to the amount of displacement during a single faulting event. The conclusion that the earthquake-induced local strain field can be detected directly by magnetic fabrics suggests that the AMS method may be used for determining the fault-plane solutions of past earthquakes, the full tensor of the local strain fields and the shape of the damage zones that surround faults.

ACKNOWLEDGEMENTS

This research was supported by the Israel Science Foundation (ISF grant No. 1245/11). We are grateful to Y. Harlavan for supportive discussion and help in analyzing the geochemical data. Thorough and helpful reviews of G. Borradiale and M. Mattei, C. Aubourg, M. Chadima and the Editor E. Petrovsky are highly appreciated.

REFERENCES

Allmendinger, R.W., 2001. FaultKinWinFull versión 1.2.2. A program for fault slip data for Windows™ computers. Available at: http://www.geo.cornell.edu/geology/faculty/RWA/programs.html.

Alsop, G.I. & Marco, S., 2012. A large-scale radial pattern of seismogenic slumping towards the Dead Sea Basin, *J. geol. Soc.,* **169,** 99–110.

Arkin, Y., 1986. Deformation of laminated sediments of the Dead Sea, in *Lecture Notes in Earth Science, No. 14, Rock and Soil Rheology,* pp. 273–277, eds Cristescu, N. & Ene, H., Springer.

Aubourg, C. *et al.*, 2004. Post-Miocene shortening pictured by magnetic fabric across the Zagros-Makran syntaxis (Iran), *Geol. Soc. Am. Spec. Paper,* **383,** 17–40.

Aubourg, C., Smith, B., Eshraghi, A., Lacombe, O., Authemayou, C., Amrouch, K., Bellier, O & Mouthereau, F., 2010. New magnetic fabric data and their comparison with palaeostress markers in the Western Fars Arc (Zagros, Iran): tectonic implications, *Geol. Soc. Lond. Spec. Publ.,* **330,** 97–120.

Bala, A., Raileanu, V., Zihan, I., Ciugudean, Viorica. & Grecu, B., 2006. Physical and dynamic properties of the shallow sedimentary rocks in the Bucharest metropolitan area, *Roman. Rep. Phys.,* **58**(2), 221–250.

Balsley, J.R & Buddington, A.F., 1960. Magnetic susceptibility anisotropy and fabric of some dirondack granites and orthogneisses, *Am. J. Sci.,* **258-A,** 6–20.

Bartov, Y., Stein, M., Enzel, Y., Agnon, A. & Reches, Z., 2002. Lake levels and sequence stratigraphy of Lake Lisan, the late Pleistocene precursor of the Dead Sea, *Quarter. Res.,* **57,** 9–21.

Beck, C., 2009. Late Quaternary lacustrine paleo-seismic archives in northwestern Alps: examples of earthquake-origin assessment of sedimentary disturbances, *Earth-Sci. Rev.,* **96,** 327–344.

Ben-Zion, Y. & Shi, Z., 2005. Dynamic rupture on a material interface with, spontaneous generation of plastic strain in the bulk, *Earth planet. Sci. Lett.,* **236,** 486–496.

Borradaile, G.J., 1987. Anisotropy of magnetic susceptibility: rock composition versus strain, *Tectonophysics,* **138,** 327–329.

Borradaile, G.J., 1991. Correlation of strain with anisotropy of magnetic susceptibility (AMS), *Pure appl. Geophys.,* **135,** 15–29.

Borradaile, G.J. & Hamilton, T.D., 2004. Magnetic fabrics may proxy as neotectonic stress trajectories, Polis Rift, Cyprus, *Tectonics,* **23,** 1–11.

Borradaile, G.J. & Henry, B., 1997. Tectonic applications of magnetic susceptibility and its anisotropy, *Earth. Sci. Rev.,* **42,** 49–93.

Borradaile, G.J. & Jackson, M., 2004. Anisotropy of magnetic susceptibility (AMS): magnetic petrofabrics of deformed rocks, in *Magnetic Fabric Methods and Applications,* Vol. 238, pp. 299–360, eds Martin-Hernández, F., Lüneburg, C.M., Aubourg, C. & Jackson, M., The Geological Society of London, Special Publications.

Borradaile, G.J. & Jackson, M., 2010. Structural geology, petrofabrics and magnetic fabrics (AMS, AARM, AIRM), *J. Struct. Geol.,* 1519–1551.

Braathen, A., Tveranger, J., Fossen, H., Skar, T., Cardozo, N., Semshaug, S.E., Bastesen, E. & Sverdrup, E., 2009. Fault facies and its application to sandstone reservoirs, *Am. Assoc. Petrol. Geol. Bull.,* **93,** 891–917.

Chester, F.M. & Logan, J.M., 1986. Implications for mechanical-properties of brittle faults from observations of the Punchbowl Fault Zone, California, *Pure appl. Geophys.,* **124,** 79–106.

Childs, C., Manzocchi, T., Walsh, J.J., Bonson, C.G., Nicol, A. & Schopfer, M.P.J., 2009. A geometric model of fault zone and fault rock thickness variations, *J. Struct. Geol.,* **31,** 117–127.

Cifelli, F., Rossetti, M., Mattei & Hirt, A.M., 2004. An AMS, structural and paleomagnetic study of Quaternary deformation in eastern Sicily, *J. Struct. Geol.,* **26,** 29–46.

Cifelli, F., Mattei, M., Chadima, M., Hirt, A. & Hansen, A., 2005. The origin of tectonic lineation in extensional basins: combined neutron texture and magnetic analyses on undeformed clays, *Earth planet. Sci. Lett.,* **235,** 62–78.

Cifelli, F., Mattei, M., Rashid, H. & Ghalamghash, J., 2013. Right-lateral transpressional tectonics along the boundary between Lut and Tabas blocks (Central Iran), *Geophys. J. Int.,* **193,** 1153–1165.

Cowie, P.A. & Scholz, C.H., 1992. Physical explanation for the displacement length relationship of faults using a post-yield fracture-mechanics model, *J. Struct. Geol,* **14,** 1133–1148.

Dugdale, D.S., 1960. Yielding of steel sheets containing slits, *J. Mech. Phys. Sol.,* **8,** 100–104.

Eyal, Y., 1996. Stress field fluctuations along the Dead Sea Rift since the Middle Miocene, *Tectonics,* **15,** 157–170.

Faulkner, D.R., Jackson, C.A.L., Lunn, R.J., Schlische, R.W., Shipton, Z.K., Wibberley, C.A.J. & Withjack, M.O., 2010. A review of recent developments concerning the structure, mechanics and fluid flow properties of fault zones, *J. Struct. Geol*., **32,** 1557–1575.

Faulkner, D.R., Mitchell, T.M., Jensen, E. & Cembrano, J., 2011. Scaling of fault damage zones with displacement and the implications for fault growth processes, *J. geophys. Res.,* **116**(B5), 1–11.

Fukuyama, E., 2009. *Fault-Zone Properties and Earthquake Rupture Dynamics,* 1st edn, Academic Press, 336 pp.

Garcıa-Lasanta, C., Oliva-Urcia, B., Román-Berdiel, T., Casas, A & P´erez-Lorente, F., 2013. Development of magnetic fabric in sedimentary rocks: insights from early compactional structures, *Geophys. J. Int.,* **194**(1), 182–199.

Garfunkel, Z., 1981. Internal structure of the Dead Sea leaky transform in relation to plate kinematics, *Tectonophysics,* **80,** 81–108.

Haase-Schramm, A., Goldstein, S.L. & Stein, M., 2004. U-Th dating of Lake Lisan aragonite (late Pleistocene Dead Sea) and implications for glacial East Mediterranean climate change, *Geoch. Cosmoch. Act,* **68,** 985–1005.

Hirt, A.M., Julivert, M. & Soldevila, J., 2000. Magnetic fabric and deformation in the Navia–Alto Sil slate belt, northwestern Spain, *Tectonophysics,* **320,** 1–16.

Housen, B.A. & Kanamatsu, T., 2003. Magnetic fabrics from the Costa Rica margin: sediment deformation during the initial dewatering and underplating process, *Earth planet. Sci. Lett.,* **206,** 215–228.

Hrouda, F., 1982. Magnetic-anisotropy of rocks and its application in geology and geophysics, *Geophys. Surv.,* **5**(1), 37–82.

Hrouda, F., Krejčí, O., Potfaj, M & Stráník, Z., 2009. Magnetic fabric and weak deformation in sandstones of accretionary prisms of the Flysch and Klippen belts of the West Carpathians: mostly offscraping indicated, *Tectonophysics,* **479,** 254–270.

Jaeger, J.C. & Cook, N.G.W., 1979. *Fundamentals of Rock Mechanics, Science Paperbacks*, Vol. 18, Chapman and Hall.

Jelinek, V., 1978. Statistical processing of anisotropy of magnetic susceptibility measured on group of specimen, *Stud. Geophys. Geod.,* **22,** 50–62.

Jelinek, V., 1981. Characterization of magnetic fabric of rocks, *Tectonophysics,* **79,** 63–67.

Katz, A., Sass, E., Starinsky, A. & Holland, H.D., 1972, Strontium behavior in the aragonite-calcite transformation: an experimental study, *Geochim. Cosmochim. Acta.,* **36,** 481–496.

Kissel, C., Barrier, E. & Laj, C., 1986. Magnetic fabric in "undeformed" marine from compressional zones, *Tectonics,* **5,** 769–781.

Larrasoaña, J.C., Gómez-Paccard, M., Santiago, G. & Roberts, A.P., 2011. Rapid locking of tectonic magnetic fabrics in weakly deformed mudrocks, *Tectonophysics,* **507,** 16–25.

Latta, D.K. & Anastasio, D.J., 2007. Multiple scales of mechanical stratification and décollement fold kinematics, Sierra Madre Oriental Foreland, northeast Mexico, *J. Struct. Geol.,* **29,** 1241–1255.

Levi, T. & Weinberger, R., 2011. Magnetic fabrics of diamagnetic rocks and the strain field associated with the Dead Sea Fault, northern Israel, *J. Struct. Geol* **33,** 566–578.

Levi, T., Weinberger, R., AIFA, T., Eyal, Y. & Marco, S., 2006a. Earthquake-induced clastic dikes detected by anisotropy of magnetic susceptibility, *Geology,* **34,** 68–71.

Levi, T., Weinberger, R., AIFA, T., Eyal, Y. & Marco, S., 2006b. Injection mechanism of clay-rich sediments into dikes during earthquakes, *Geochem. Geophys. Geosyst,* **7,** 1–20.

Liu, B., Saito, Y., Yamazaki, T., Abdeldayem, A., Oda, H., Hori, K. & Zhao, Q., 2001. Paleocurrent analysis for the Late Pleistocene-Holocene incised-valley fill of Yangtze delta, China by using anisotropy of magnetic susceptibility data, *Marine Geol.,* **176,** 175–189.

Lyakhovsky, V. & Ben-Zion, Y., 2008. Scaling relations of earthquakes and aseismic deformation in a damage rheology model, *Geophys. J. Inter.,* **172,** 651–662.

Ma, S. & Andrews, D.J., 2010. Inelastic off-fault response and three-dimensional dynamics of earthquake rupture on a strike-slip fault, *J. geophys. Res.,* **115,** B04304, doi:10.1029/2009JB006382.

Marco, S. & Agnon, A., 1995. Prehistoric earthquake deformation near Masada, Dead Sea graben, *Geology,* **23,** 695–698.

Marco, S. & Agnon, A., 2005. High-resolution stratigraphy reveals repeated earthquake faulting in the Masada Fault Zone, Dead Sea Transform, *Tectonophysics,* **408,** 101– 112.

Marco, S., Stein, M., Agnon, A. & Ron, H., 1996. Long term earthquake clustering: a 50 000 year paleoseismic record in the Dead Sea graben, *J. geophys. Res.,* **101,** 6179– 6192.

Marco, S., Ron, H., McWilliams, M.O. & Stein, M., 1998. High-resolution record ofgeomagnetic secular variation from Late Pleistocene Lake Lisan sediments (paleo Dead Sea), *Earth planet. Sci. Lett.,* **161,** 145–160.

Mattei, M., Sagnotti, L., Faccenna, C. & Funiciello, R., 1997. Magnetic fabric of weakly deformed clay-rich sediments in the Italian peninsula: relationship with compressional and extensional tectonics, *Tectonophysics,* **271,** 107–122.

Nagata, T., 1961. *Rock Magnetism,* Maruzen.

Nowaczyk, N.R., 2011. Dissolution of titanomagnetite and sulphidization in sediments from Lake Kinneret, Israel, *Geophys. J. Int.,* **187,** 34–44.

Othman, A.A.A., 2005. Construed geotechnical characteristics of foundation beds by seismic measurements, *J. geophys. Eng.,* **2,** 126–138.

Parés, J.M. & van der Pluijm, B.A., 2003. Magnetic fabric and strain in pencil structures of the Knobs Formation, Valley and Rudge Province, US Appalachians, *J. Struct. Geol.,* **25,** 1349–1358.

Parés, J.M., van der Pluijm, B.A & Turell, J.D., 1999. Evolution of magnetic fabrics during incipient deformation of mudrocks (Pyrenees, northern Spain), *Tectonophysics,* **307,** 1–14.

Porreca, M. & Mattei, M., 2012. AMS fabric and tectonic evolution of Quaternary intramontane extensional basins in the Picentini Mountains (Southern Apennines, Italy), *Int. J. Earth. Sci.,* **101,** 787–802.

Rees, A.I., 1966. The effects of depositional slopes on the anisotropy of magnetic susceptibility of laboratory deposited sands, *J. Geol.,* **74,** 856–867.

Rees, A.I., 1971. The magnetic fabric of a sedimentary rock deposited on a slope, *J. Sediment. Petrol.,* **41,** 307–309.

Rees, A.I. & Woodall, W.A., 1975. The magnetic fabric of some laboratory-deposited sediments, *Earth planet. Sci. Lett.,* **25,** 121–130.

Rice, J.R., Sammis, C.G. & Parsons, R., 2005. Off-fault secondary failure induced by a dynamic slip pulse, *Bull. seism. Soc. Am.,* **95,** 109–134.

Roberts, A.P., Chang, L., Rowan, C.J., Horng, C.S. & Florindo, F., 2011. Magnetic properties of sedimentary greigite (Fe_3S_4): An update, *Rev. Geophys*., **49,** RG1002, 1–46.

Rochette, P., Jackson, M.J. & Aubourg, C., 1992. Rock magnetism and the interpretation of anisotropy of magnetic susceptibility, *Rev. Geophys.,* **30,** 209–226.

Ron, H., Nowaczyk, N.R., Frank, U., Marco, S. & McWilliams, M.O., 2006. Magnetic properties of Lake Lisan and Holocene Dead Sea sediments and the fidelity of chemical and detrital remanent magnetization, in *GSA Book New Frontiers in Dead Sea Paleoenvironmental Research,* pp. 171–182, eds Enzel, Y., Agnon, A. & Stein, M., GSA Special Paper 401.

Sagy, A., Reches, Z & Agnon, A., 2003. Hierarchic three-dimensional structure and slip partitioning in the western Dead Sea pull-apart, *Tectonics,* **22**(4), 1–17.

Scholz, C.H., 2002. *The Mechanics of Earthquakes and Faulting,* 2nd edn, Cambridge Univ. Press, 439 pp.

Schultz, R.A. & Fossen, H., 2008. Terminology for structural discontinuities, *Am. Assoc. Petrol. Geol. Bull.,* **92,** 853–867.

Schwehr, K. & Tauxe, L., 2003. Characterization of soft sediment deformation: detection of cryptoslumps using magnetic methods, *Geology,* **31,** 203–206.

Shearer, P.M., 1999. *Introduction to Seismology,* Cambridge Univ. Press, 260 pp.

Shipton, Z.K. & Cowie, P.A., 2003. A conceptual model for the origin of fault damage zone structures in high-porosity sandstone, *J. Struct. Geol.,* **25,** 333–344.

Sneh, A. & Weinberger, R., 2014. Major structures of Israel and environs, scale 1:500 000, *Isr. Geol. Surv*.

Soto, R., Casas-Sainz, A.M., Villalaín, J.J. & Oliva-Urcia, B., 2007. Mesozoic extension in the Basque–Cantabrian basin (N Spain):c from AMS and brittle mesostructures, *Tectonophysics,* **445,** 373–394.

Stacey, F.D., 1960. Magnetic anisotropy of igneous rocks, *J. geophys. Res.,* **65,** 242–2442.

Taira, A., 1989. Magnetic fabrics and depositional processes, in *Sedimentary Facies in the Active Plate Margin,* pp. 43–47, eds Taira, A. & Masuda, F.. TERRAPUB, Tokyo.

Tarling, H.D. & Hrouda, F., 1993. *The Magnetic Anisotropy of Rocks*, Chapman & Hall.

Tauxe, L., 1998. *Paleomagnetic Principles and Practice*: Kluwer Academic Publishers, 299 pp.

Tauxe, L., Kylstra, N. & Constable, C., 1991. Bootstrap statistics for paleomagnetic data, *J. geophys. Res.,* **96,** 11 723–11 740.

Torabi, A. & Berg, S.S., 2011. Scaling of fault attributes: a review, *Mar. Petrol. Geol.,* **28,** 1444–1460.

Turcotte, D.L. & Schubert, G., 1982. *Geodynamics: Application of Continuum Physics to Geological Problems,* John Wiley, 450 pp.

Turcotte, D.L. & Schubert, G., 1985. *Geodynamics: Application of Continuum Physics to Geological Problems,* John Wiley.

Tveranger, J., Cardozo, N., Kjeldaas, G.C., Nøttveit, H. & Røe, P., 2008. Volumetric fault zone modelling using fault facies, in *Proceedings of the Fault Zones: Structure Geomechanics and Fluid Flow Conference,* The Geol. Soc., London.

Twiss, R.J. & Moores, E.M., 1992. *Structural Geology*, W.H. Freeman and Company, 532 pp.

Weinberger, R., Lyakhovsky, V., Baer, G. & Agnon, A., 2000. Damage zones around en echelon dike segments in porous sandstone, *J. geophys. Res.,* **105**(B2), 3115–3133

Yukutake, Y., Iio, Y. & Horiuchi, S., 2010. Detailed spatial changes in the stress field of the 1984 western Nagano earthquake region, *J. geophys. Res.,* **115**(B6), 1–17.

SUPPORTING INFORMATION

Additional Supporting Information may be found in the online version of this article:

Supplementary Data item I. Plot of Lisan hysteresis parameters (Day *et al.* 1977) Modified after Ron *et al.* (2006). Mrs – saturation of remanence; Ms –saturation magnetization; Bc – coercitiy field; Bcr – coercivity of remanence; SD – single domain; MD – multidomain; PSD – pseudo-single domain. Open circles refer to the residual material that remained after extracting the magnetic grains (open triangle) from detritus material (solid circles). Jrs – saturation of remanence; Js – J saturation.

Supplementary Data item II. 95% ellipse confidence of k_1 axes versus distance from fault planes. Red and blue circles mark fabrics characterized by well-grouped AMS axes and weakly grouped k_1 and k_2 axes, respectively.

Supplementary Data item III, **Table 1.** XRD data in sites MM and MP.

Supplementary Data item IV. %$CaCO_3$ versus Sr content of 13 selected samples from sites MM and MP. Red diamonds and blue circles represent 'deformation fabrics' and 'deposition fabrics', respectively.

Supplementary Data item V. k_m values of the three studied sites and the reference outcrops in Ami'az Plain. Red and blue circles represent 'deformation fabrics' and 'deposition fabrics', respectively. Numbers in squares indicate the average k_m values of the 'deformation fabrics' and 'deposition fabrics' in individual studied sites.

Supplementary Data item VI. Static stress condition presented by the Coulomb criterion (Jaeger & Cook 1979) during rupturing under the Lisan lake-water column. The values of relevant variables and calculated parameters are indicated. (http://gji.oxfordjournals.org/lookup/suppl/doi:10.1093/gji/ggu300/-/DC1)

Please note: Oxford University Press is not responsible for the content or functionality of any supporting materials supplied by the authors. Any queries (other than missing material) should be directed to the corresponding author for the article.